IMPLEMENTATION OF A SPHERICAL DOUBLE PLASMA-MIRROR TELESCOPE FOR A MULTI-PETAWATT LASER

V. SCUTELNIC,[1,‡,] M. SPEICHER,[1,‡] A. FAZZINI,[1] P. GHENUCHE,[2] D. DORIA,[2] A. AILINCUTEI,[3] B. GONZALEZ- IZQUIERDO,[1] T. ASAVEI,[2] S. BALASCUTA,[2] J.J. BEKX,[1] P.-G. BLEOTU,[2] G. BODINI,[1] C. BRAGANZA,[1] A. F. BRODERSEN,[1] A. CAVALLI,[1] O. CHALUS,[3] G. COJOCARU,[3] J. D'MELLO,[1] I. DANCUS,[2] C. DERYCKE,[3] F. DEURVORST,[1] M. EHRMANNTRAUT,[1] D. GENGENBACH,[1] D.G. GHITA,[2] L. GIUFFRIDA,[4] M. GUGIU,[2] M. M. GÜNTHER,[1] O. JUINA,[1] K. KENNEY,[1] S. KUMAR,[1] M. MARTINEZ-PACHECO,[1] I. MINGUEZ BACHO,[1] S. NORBAEV,[2] N. POETRANTO,[1] H. RUHL,[1] E. SCHORK,[1] M. STEIN,[1] S. STEINKE,[1,¶] A.-M. TALPOSI,[2] A. TOMA,[2] M. TOSCA,[4,5] A. UBARHANDE,[1] L. VASESCU,[2] E. GAUL,[1] D. E. RIVAS,[1] M. S. SCHOLLMEIER[1,|] AND G. KORN[1]*

[1]Marvel Fusion GmbH, Theresienhöhe 12, 80339 Munich, Germany

[2]Extreme Light Infrastructure (ELI-NP) & Horia Hulubei National Institute for R&D in Physics and Nuclear Engineering (IFIN-HH), 30 Reactorului Street, 077125 Magurele, Romaniawind

[3]Thales LAS France, 78990 Élancourt, France

[4]ELI Beamlines Facility, The Extreme Light Infrastructure ERIC, Dolní Brežany 252 41, Czech Republic

[5]Charles University, Faculty of Mathematics and Physics, Department of Macromolecular Physics, Prague 180 00, Czech Republic.

[‡]These authors contributed equally

[¶]Until June 2023.

**valeriu.scutelnic@marvelfusion.com*

[|]marius.schollmeier@marvelfusion.com

1. Experimental details

The Extreme Light Infrastructure – Nuclear Physics (ELI-NP) laser facility recently demonstrated production of 10 PW pulses [1]. A detailed description of the high-power laser system (HPLS) architecture is given by Lureau *et al.* [2]. At the facility, two laser beam transport lines provide two different intensity regimes using long and short focal configurations. In this way, two experimental conditions are available for users: reaching up to 10^{23} W/cm^2 for solid targets at the short-focal-length interaction chamber and ~10^{20} W/cm^2 for gas phase targets in the long-focal-length interaction chamber. An intermediate of ~10^{21} W/cm^2 intensity with a large area (and corresponding long Rayleigh length), smooth focal spot was required for investigating particle acceleration from solid targets (manuscript in preparation). Consequently, this investigation has been performed at the long-focal-length chamber with the intensity boost by the DPM system.

The DPM setup consists of eleven plasma mirror pairs installed on a compact (40 cm diameter) wheel, which permits a facile exchange between the shots on target (see Section 3 of SI for a mechanical drawing) without breaking the vacuum in the target chamber. Baffles are added between the pairs to screen the unused mirror pairs from ablated material upon interaction of the laser with the glass substrate. An investigation into the material sputtering on the plasma mirrors is given in Section 3.6 of SI.

The laser energy has been measured at a laser diagnostic bench using leakage from the compressor mirror. The pulse duration is measured with a FROG setup on-shot at the experimental chamber (see Section 6 of SI).

Ashland (https://www.ashland.com) GafChromic HD-V2 and EBT3 films, were used in the RCF detector.

2. Simulation details

Physical Optics Propagation is used to simulate diffraction effects. For this, a coherent optical beam at the central wavelength of the laser (810 nm) is propagated through the optical system. A top hat beam type and 1024x1024 grid was used to sample the beam.

Standard spot diagrams are simulated by tracing bundles of rays through the optical system to the focal plane to show ray distributions. The Airy disk radius is calculated as 1.22 times the central wavelength of the laser multiplied by the F/# of the system.

The point spread function is computed using direct integration of the Huygens wavelets method, a grid of 256x256 pixels was used for sampling the pupil and image. The Strehl ratio is computed by dividing the peak intensity of the point spread function with and without considering aberrations. The wavelengths and their weight are chosen to reproduce the experimentally measured spectrum of the laser, the discretization step in the simulation is 5 nm.

Spherical, coma, astigmatism, field curvature, distortion, longitudinal and transversal color coefficients in the Seidel diagram are computed and displayed for each surface in the optical system.

3. Double-plasma mirror (DPM) optical system

3.1 Higher-order reflections on the plasma mirrors

During alignment the laser intensity is low and the front surfaces of the plasma mirrors are highly transmissive, leading to multiple reflections from the back surfaces that are also directed towards the main focal plane. Figure S1 depicts the result of a non-sequential ray tracing simulation, where rays after each reflection are represented with a different color. To ensure all these reflections have negligible intensity on target, we use AR coating on both front and back surfaces of the mirrors.

The target mount has been designed in the way that the ghost reflections do not reach the neighboring targets.

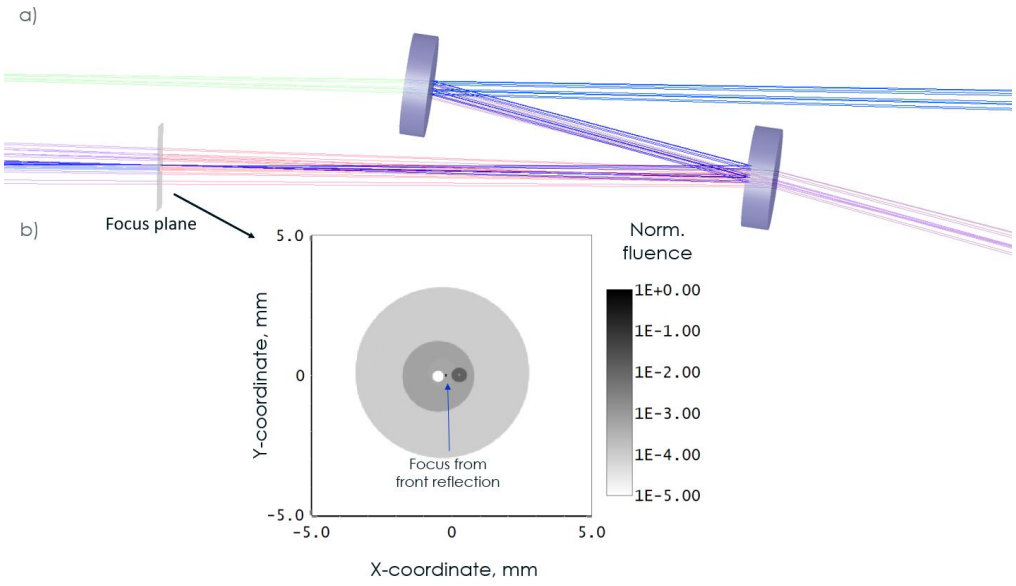

Figure S1. (a) Rays originating from reflections at front surfaces of the plasma mirrors are shown in bright blue color. Reflections involving the back surfaces are shown in faint colors. (b) Intensity distribution at the focal plane. The fluence distribution of reflections involving back surfaces is >2 orders of magnitude lower than for the main focus before the plasma mirror is triggered.

3.2 Laser intensity on plasma mirrors

The simulated intensity on the plasma mirrors for a pulse power of 10 PW in the F/19.4 configuration is shown in Figures S2 and S3.

The full width at half maximum (FWHM) of the beam on PM1 measures 2.6 mm in diameter.

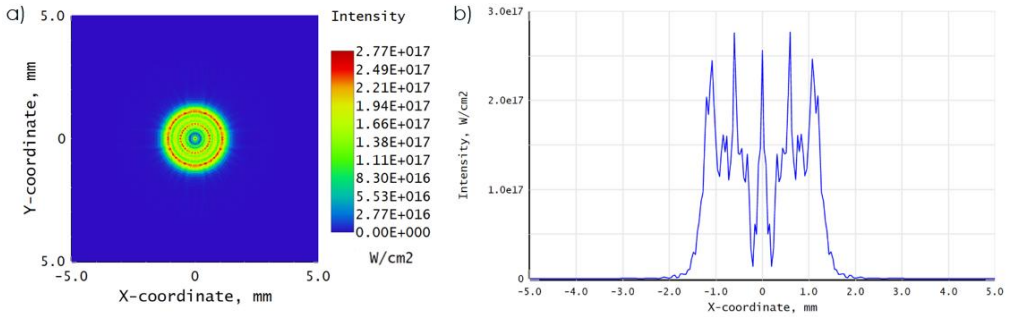

Figure S2. Beam profile on PM1, DPM is configured for F/19.4. (a) 2-D intensity map. (b) Line-out across the center-axis for the intensity profile.

The FWHM of the beam on PM2 measures 3.4 mm in diameter (see Figure S3). An average reflectivity of PM1 equal to square root of total DPM reflectivity $\sqrt{0.68}$ is used in the simulation.

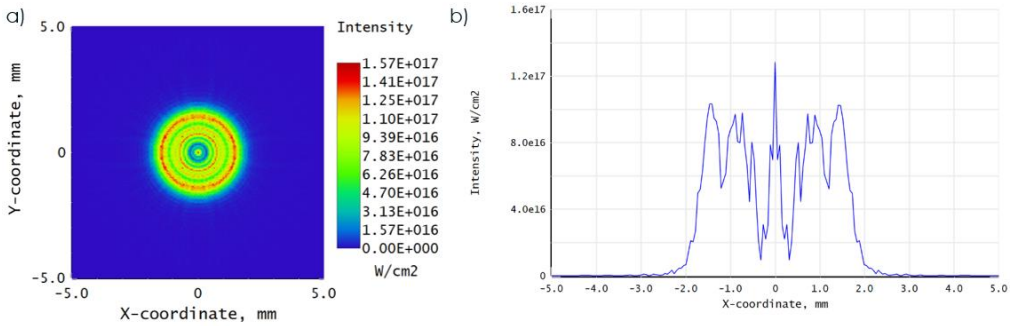

Figure S3. Beam profile on PM2, DPM is configured for F/19.4. (a) 2-D intensity map. (b) Line-out across the center-axis for the intensity profile.

3.3 Laser contrast measurement

The laser contrast without plasma mirrors is measured with a third order autocorrelator (TUNDRA, Ultrafast Innovations) and is shown in Figure S4. The contrast is below 10^{-7} up to -5 ps. The inherent background of this device is 10^{-9}, limiting the dynamic range. Nonetheless, a 10^{-11} contrast could be measured for delays before -100 ps [3].

The contrast measurement with plasma mirrors by means of the high-power diagnostics is hindered by the dispersion of two achromat lenses and a vacuum window that stretch the laser pulse beyond acceptable limits.

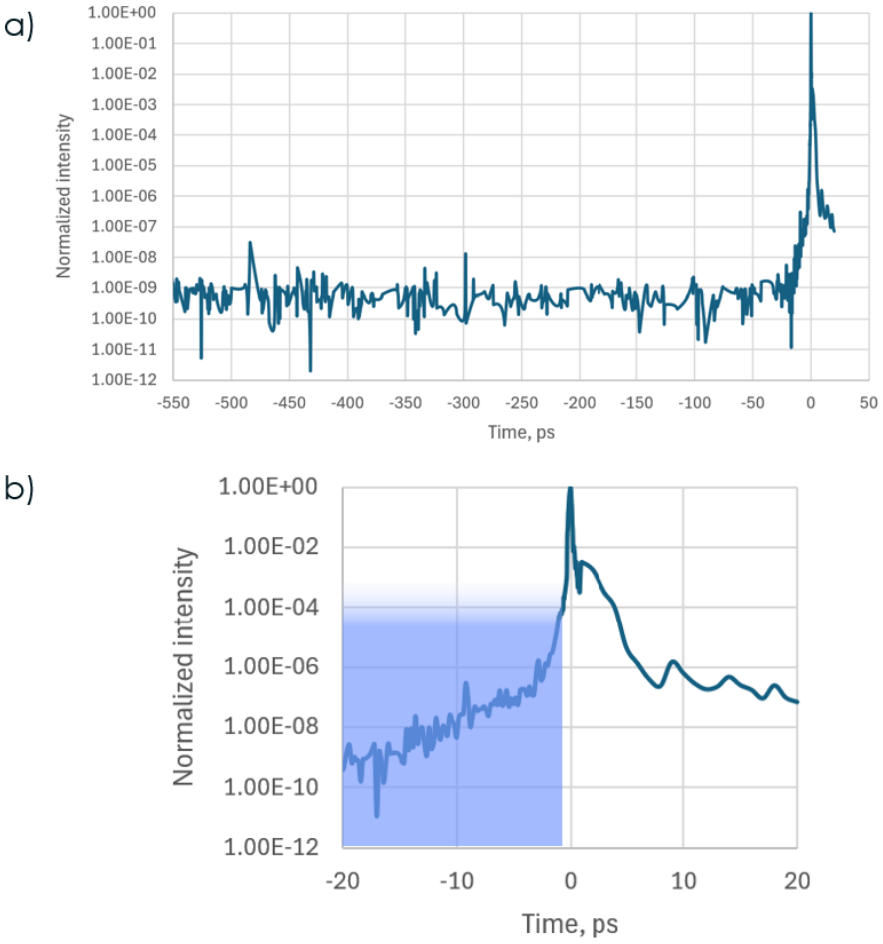

Figure S4. Picosecond contrast measurement with Tundra: (a) full range, (b) zoom on the onset of the intensity rise, the shaded area represents the laser signal that lacks sufficient intensity to trigger plasma formation and is transmitted through the plasma mirrors.

3.4 Correction of the residual astigmatism with the deformable mirror

To remove the residual aberrations in the F/19.4 configuration, the deformable mirror (DM), installed before the compressor, can be adjusted (Figure S5). In this way, a diffraction limited focus can be obtained by changing the Z_2^2 – vertical astigmatism Zernike term. Actuation of the DM motors is in the range of ±210 nm, which is well within the range of commercial DMs. The value of the theoretically predicted flexing of DM has been found to be consistent with the experiment.

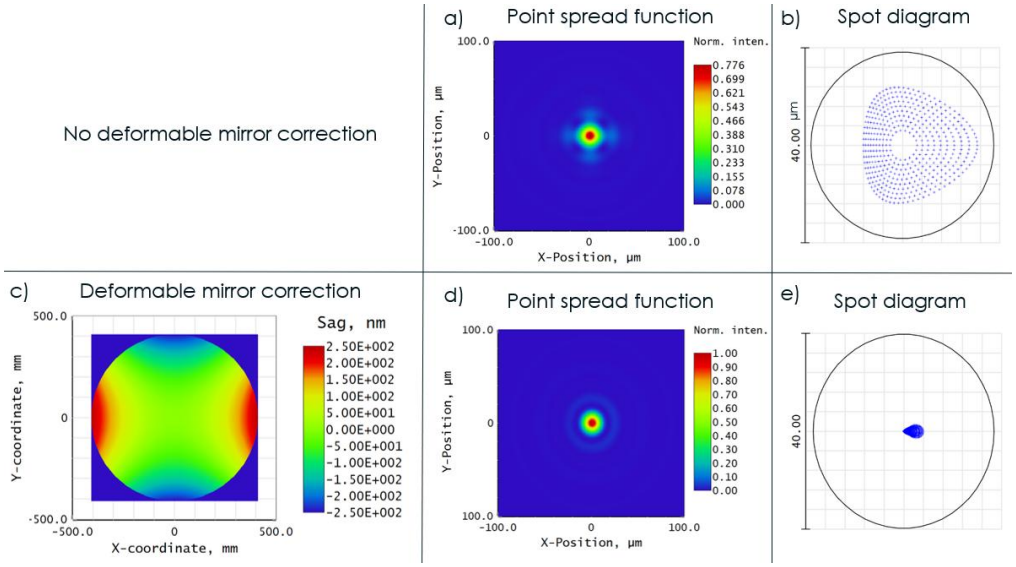

Figure S5. No deformable mirror correction: (a) Point spread function (Strehl ratio 0.776) and (b) spot diagram. Correction with the deformable mirror results in a diffraction limited focus: (c) Sag of the deformable mirror, (d) focus point spread function (Strehl ratio 0.998) and (e) spot diagram.

The wavefront map and phase map at the focal plane (Figure S6) provide a deeper insight into the role of the deformable mirror correction. The phase has been computed by means of Physical Optics Propagation.

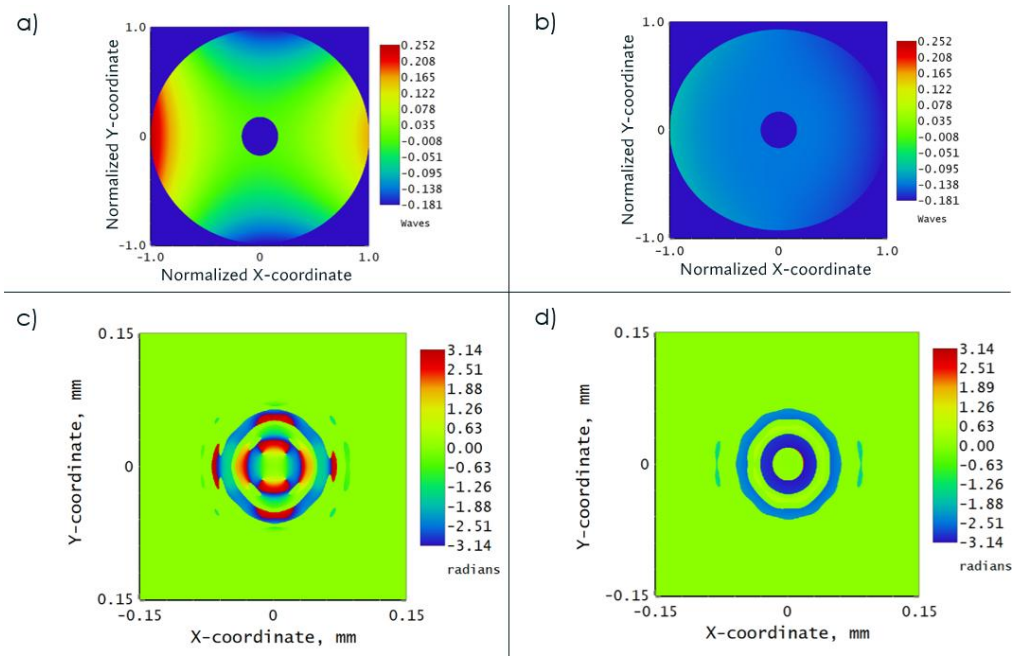

Figure S6. (a) Wavefront map at the focal plane based on ray tracing before and (b) after adjusting the deformable mirror. (c) Phase at the focal plane before and (d) after adjusting the deformable mirror.

3.5 Tunability of F/#

By changing the distance between plasma mirror 2 and F/19.4 focal plane a variable F/# of the system, and hence a variable focus size, can be achieved. The distance between the F/63.5 focus and PM1 needs to be adjusted as well to produce a sharp focus. The focal plane location can be maintained in the same position by adjusting the DPM wheel location within ±7 mm and by translating the spherical mirror (F/63.5 focus) within ±60 mm along the beam axis. In Figure S7(a-d) the point spread function is shown for the DPM system variations, illustrating the facile tunability of the focus intensity. The intensity levels off when the F/# decreases to F/16 (Figure S7e) due to the accumulated aberrations significantly reducing the Strehl ratio. However, in this case, the focus can still be optimized further by a moderate correction in the deformable mirror similar to Figure S5.

The experimentally measured distance between PM2 and the demagnified focus is 73±0.5 mm, this leads to the F/# uncertainty of 19.4±0.6.

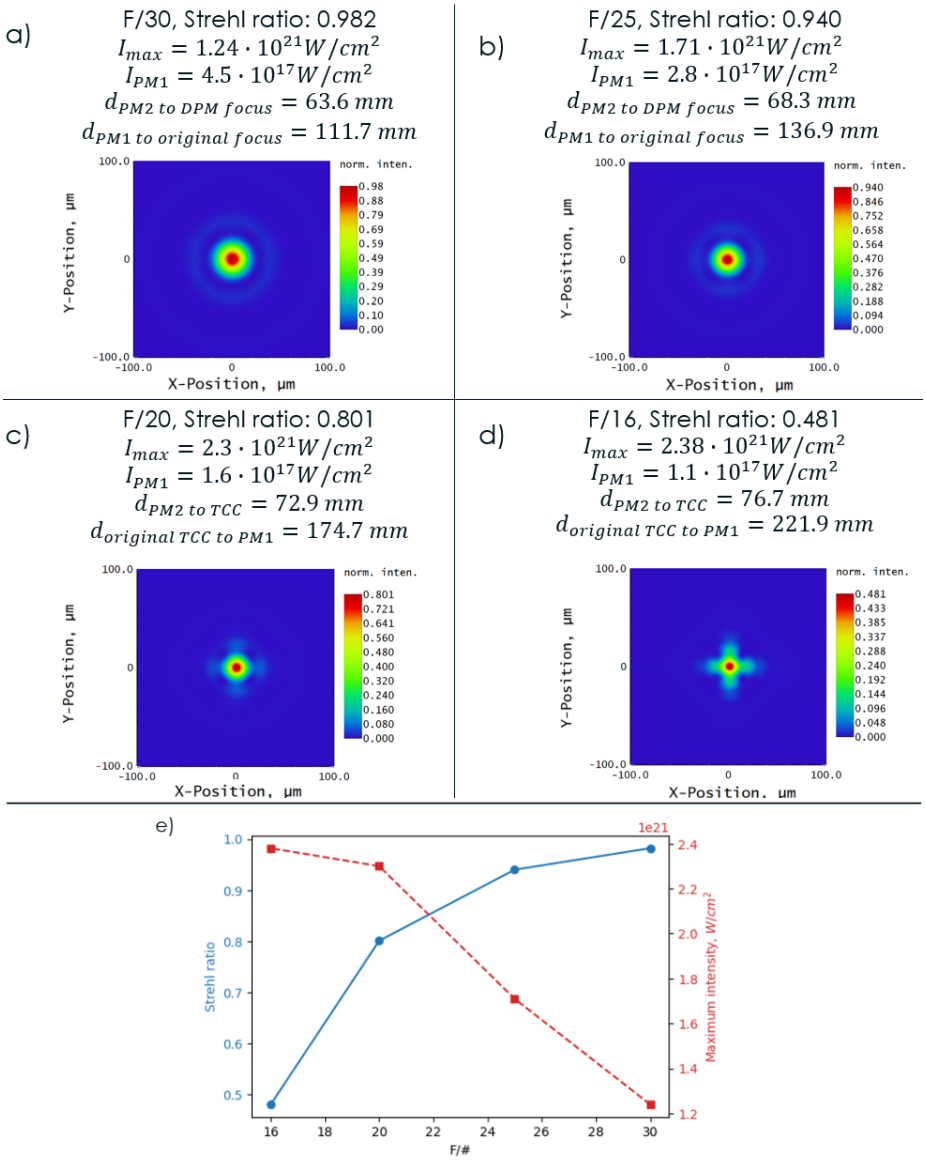

Figure S7. (a) – (d) Calculation of the point spread function (PSF) and Strehl ratio for various distances between the plasma mirror 2 and the target chamber center. The distance from plasma mirror 1 to the original focal plane has been optimized. The intensity is calculated assuming no loss of laser energy on the mirrors and 10 PW pulses, when the deformable mirror is not adjusted. Assuming the average reflectivity of the plasma mirrors to be the same as in Figure 4, the intensity on the second plasma mirror results to be from $2.0 \cdot 10^{17}$ to $4.2 \cdot 10^{16}$ W/cm^2. (e) Strehl ratio and peak intensity of the focus as a dependence of the F/# for the simulated configurations.

3.6 Micrographs of PM ablation and material deposition

PM1 and PM2 have a second large damage spot that is two times bigger than the primary damage spot (see Figure S8 and S9 for a representative case of damage on the plasma mirrors).

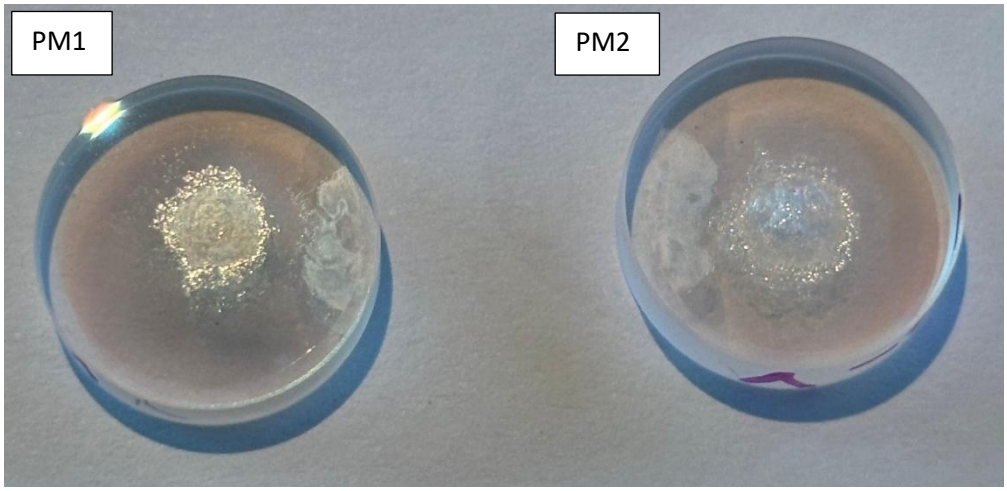

Figure S8. The laser-damaged spot size is 3.2 mm on PM1 and 3.6 mm on PM2. A larger diameter damage appears on the periphery of the mirror substrate. The DPM was configured to F/19.4 focusing.

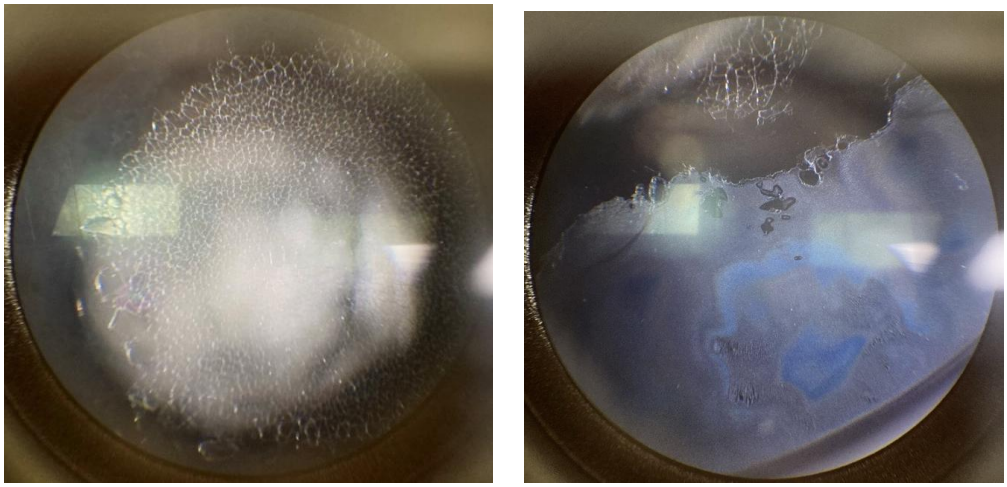

Figure S9. Left: microscope image of the surface damage at the laser beam location on PM1. The glass is shattered, and micro-cracks are created. Right: image of the sputtered side of PM1 at the edge of the substrate. The DPM was configured to F/19.4 focusing.

Upon inspection using a microscope, the different color and the color gradients of the secondary damage area indicate that the surface was coated with a thin film of another material.

An explanation is that the plasma mirror plume of PM1 hits PM2, and plasma mirror plume of PM2 hitting PM1 as sketched in Figure S10.

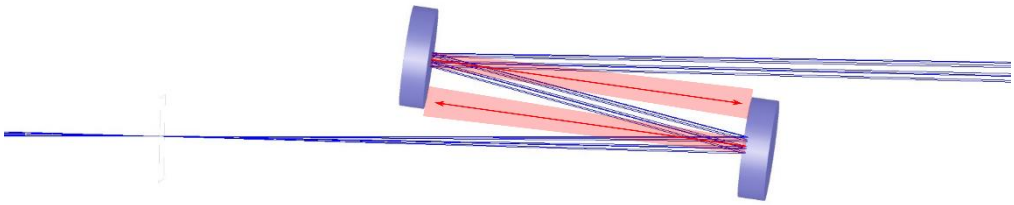

Figure S10. Plasma mirror plume from the substrate is depicted with red. The DPM was configured to F/19.4 focusing.

The diameter of the damage by the plasma plume is ~7 mm and the circle center is situated roughly at the top of PM2 and at the bottom of PM1. This implies an opening of the plasma cone of about 2 degrees. The silver layer being sputtered onto the opposite PM is well pronounced (Figure S11).

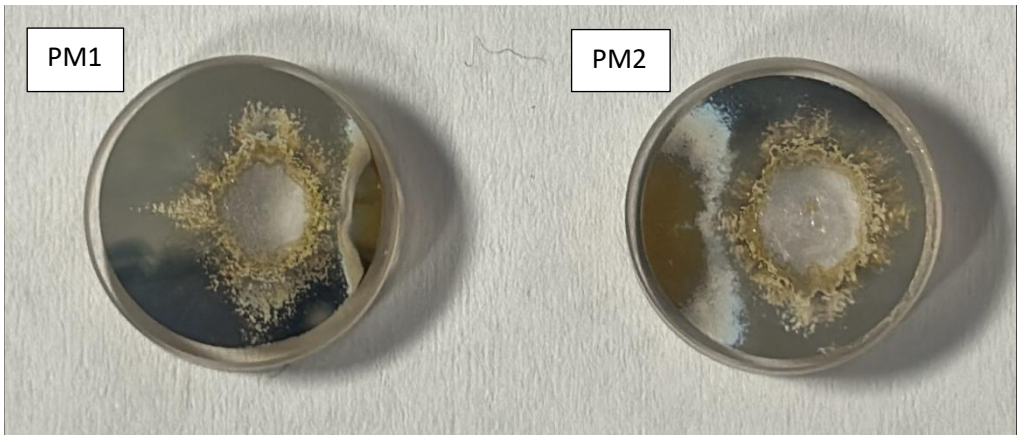

Figure S11. Image of the silver-coated DSM after shot. The DPM was configured to F/19.4 focusing.

4. Optomechanical design of double-plasma mirror and high-power diagnostics

The computer-aided design (CAD) of the double-plasma mirror is shown in Figure S12. Eleven double plasma mirror pairs are installed on a wheel that permits exchanging between the shots on target. The plasma mirror pairs are separated with baffles to prevent contamination of the neighbor mirror sets, as shown in Figures S8 and S11.

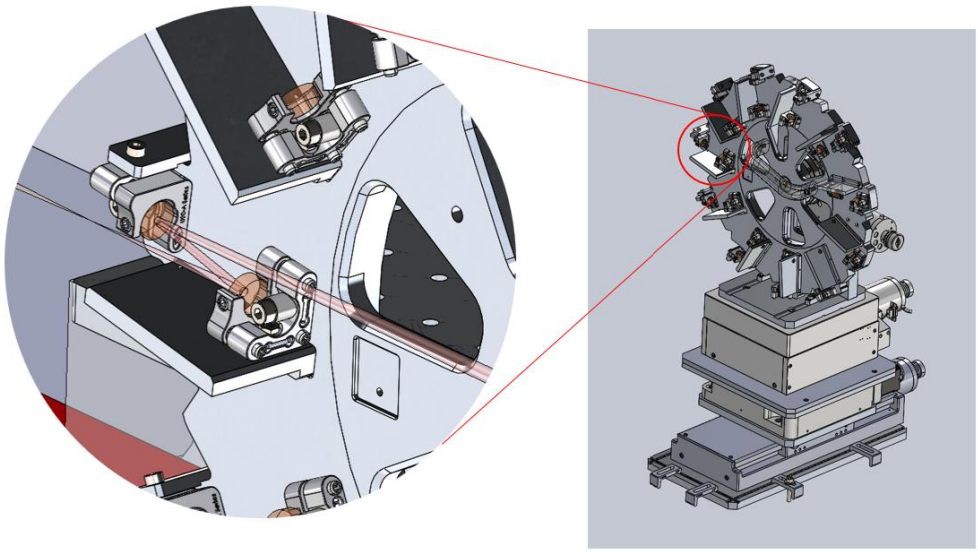

Figure S12. Mechanical implementation of the DPM wheel exchanger with two translational and two rotational axes of motion. The zoom depicts one DPM pair and the laser path towards the target chamber center. The beam is reflected in the vertical plane to ensure s-polarization of the laser on the plasma mirrors. A block is placed behind each plasma mirror to stop the transmitted light.

The complete setup of the high-power diagnostics is presented in Figure S13. M0 is a 12-inch Edmund Optics mirror substrate that is uncoated on the front (concave parabolic) surface and has an antireflecting coating (for 760-860 nm bandwidth) applied on the rear surface of the mirror. The laser beam is p-polarized on M0 impinging at 0.25° angle of incidence. The intermediate focus is imaged with a 4f relay consisting of two 1.52 m achromat lenses. The routing mirrors are silver coated, except M1, M2 and M4, which are replaced with transparent wedges to reduce the laser intensity (the beam is p-pol on the optics). The vacuum viewport has antireflective coatings for the full laser bandwidth (760-860 nm) and high optical surface quality allowing for an unperturbed transport of the beam onto the microscope table.

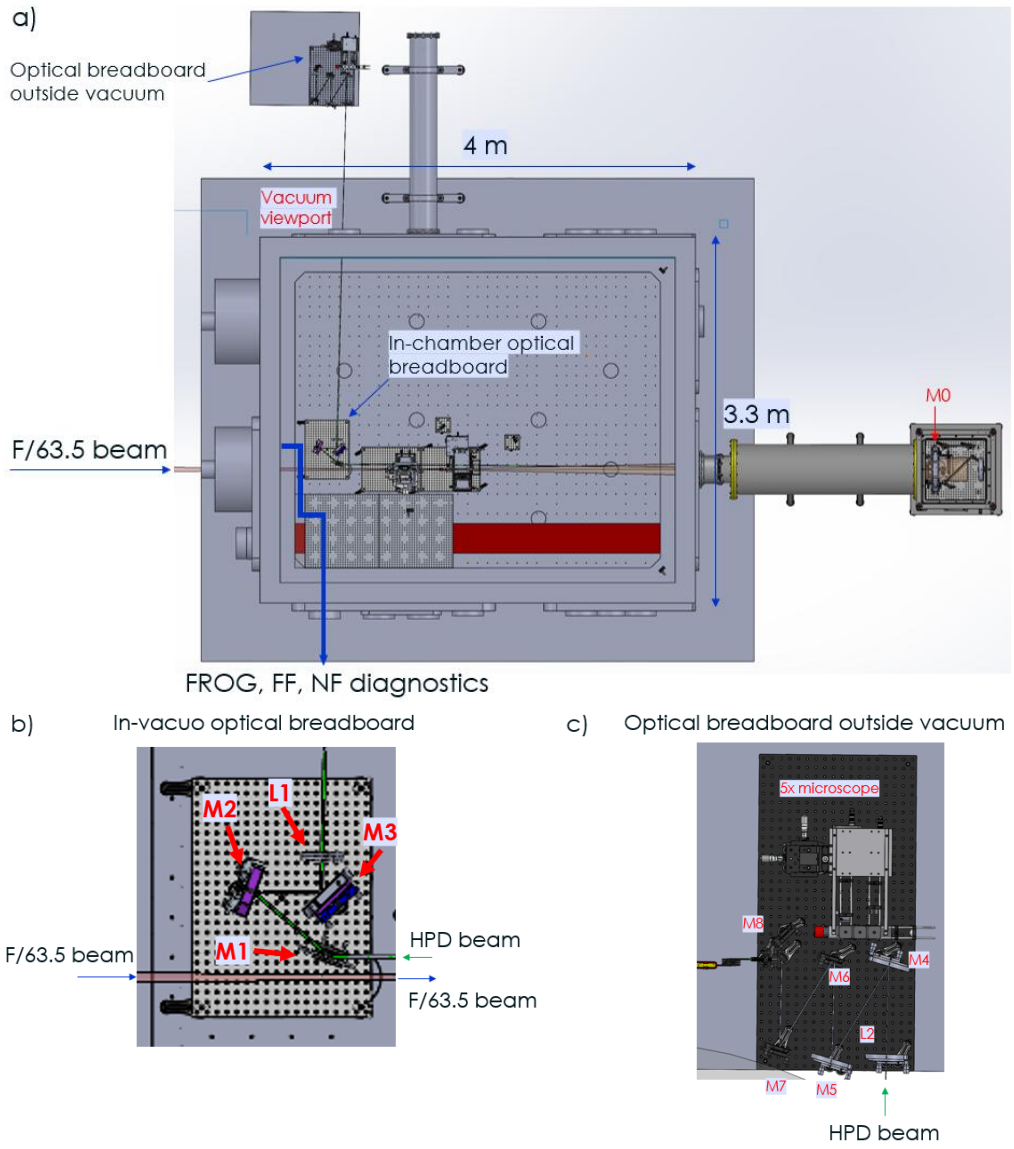

Figure S13. (a) Mechanical design of the high-power diagnostics. (b) and (c) Detailed view of the in-vacuo optical breadboard and outside vacuum chamber, respectively. Laser beam is p-polarized on the high-power diagnostic optics.

5. Background treatment in the high-power diagnostic images

Dark current on the camera is removed by subtracting an image without the laser light. An additional tilted background is derived from the four corners (100x100 pixel) of the image on shot. An example is shown in Figure S14. Background remains after simple image subtraction, as the pixel values do not oscillate around zero. A similar behavior is observed when extrapolating the mean pixel value of those corners to the full image and calculating the background contribution to the total signal.

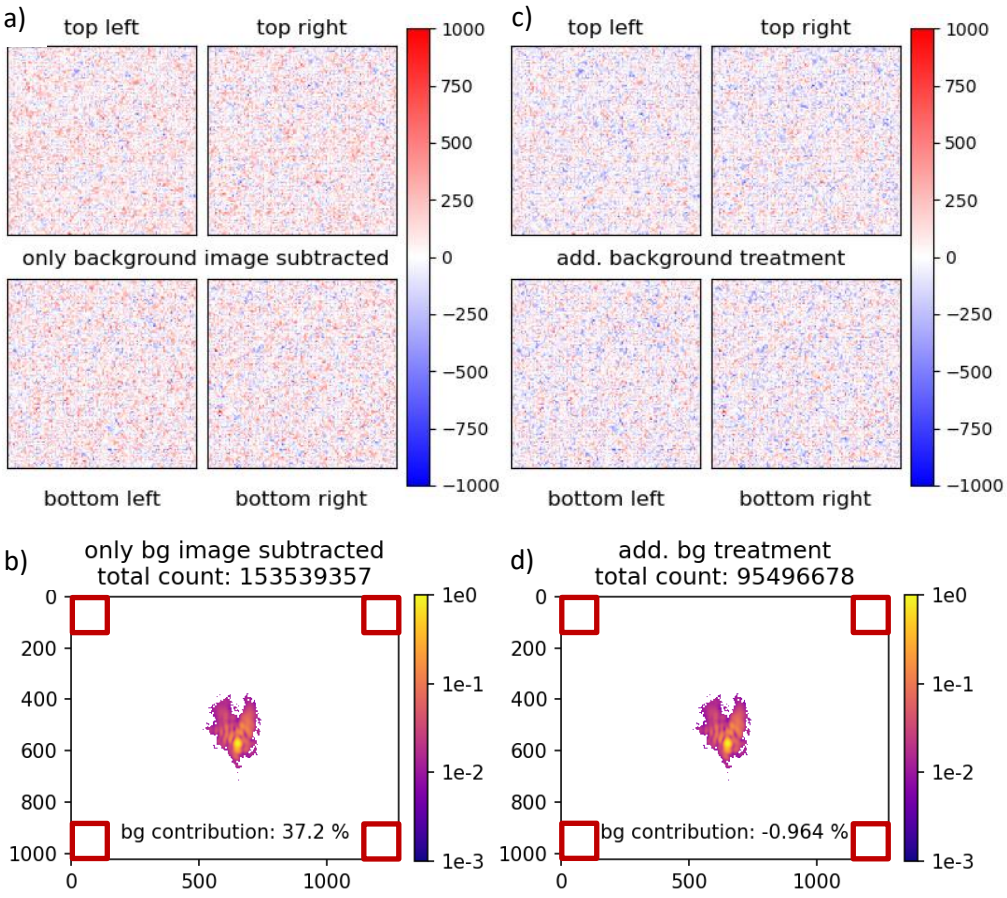

Figure S14. Comparison of the two methods of background correction. (a-b) Only the background image is subtracted. (c-d) Additional background is removed based on the extrapolation of the mean pixel values of the 4 corners of the image.

6. High-power diagnostic imaging characteristics

Imaging parameters in completion to Figure 2 are given below. The spot diagram (Figure 15a) shows that the rays from the central part of the spectrum (780-820 nm) are localized within the Airy disk, while the wavelengths at the extremities of the spectrum are the most affected by chromatic aberrations stemming from the telescope lenses. The peak-to-valley wavefront error is limited to λ/5 (Figure 15b). Modulation transfer function is given in Figure 15c. The spatial blurring is assessed with geometric image analysis (Figure 15d).

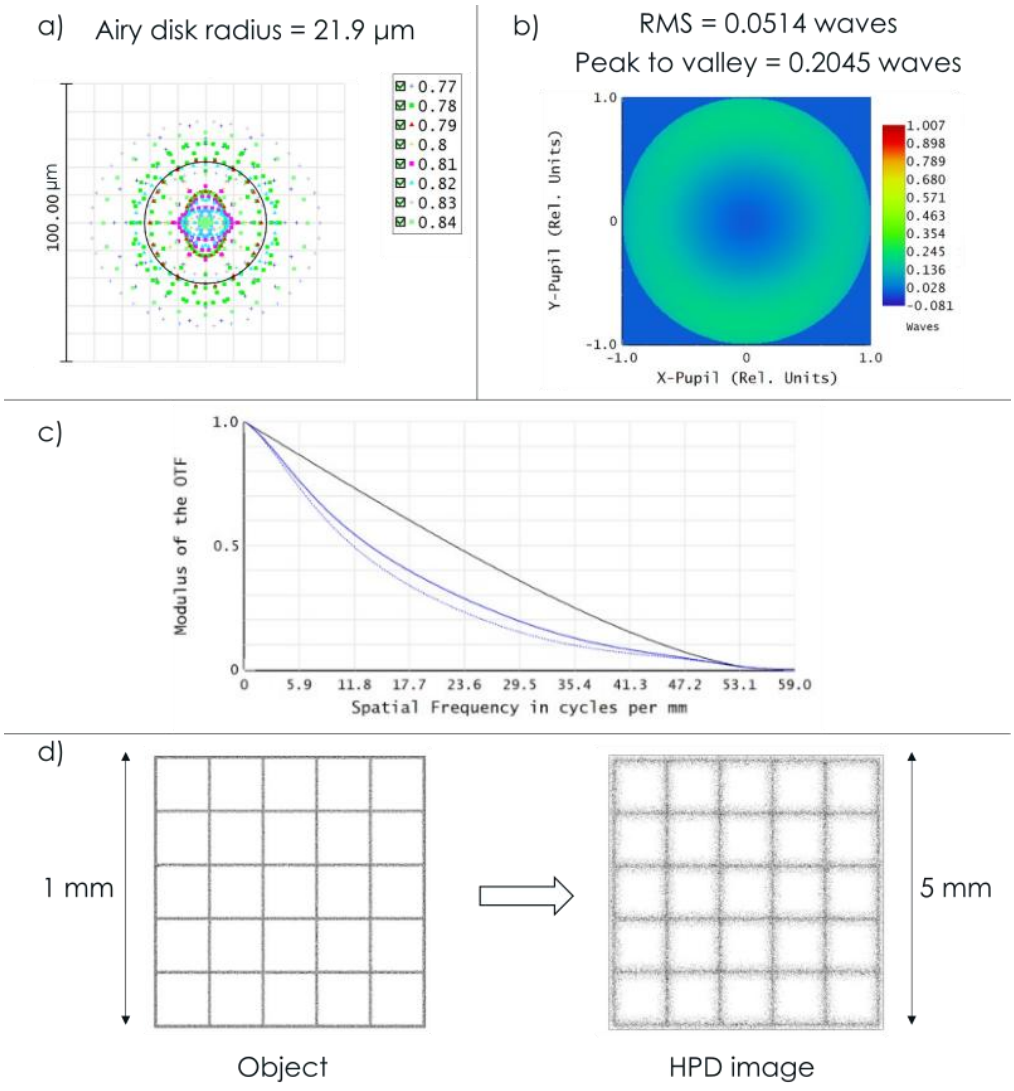

Figure S15. High-power diagnostic imaging characteristics for the demagnified focus after the DPM system. (a) Spot diagram based on rays covering the spectrum of the laser, wavelength in the legend is represented in mm. (b) Wavefront map and root-mean square deviation of the imaged focus. (c) Modulation transfer function. (d) Geometric image analysis of an object representing a 1x1 mm grid.

Seidel coefficients (Figure S16) computed for each surface give further insight into the origin of the optical aberrations of the HPD system. The sum of the aberrations clearly shows that spherical aberrations of the refocusing on-axis parabolic mirror is the dominant factor in the imaging system at the central wavelength of the laser. The spherical aberrations are well compensated in the doublet lenses of the 4-f telescope, and the chromatic aberrations are two times smaller than the spherical aberration of the refocusing mirror.

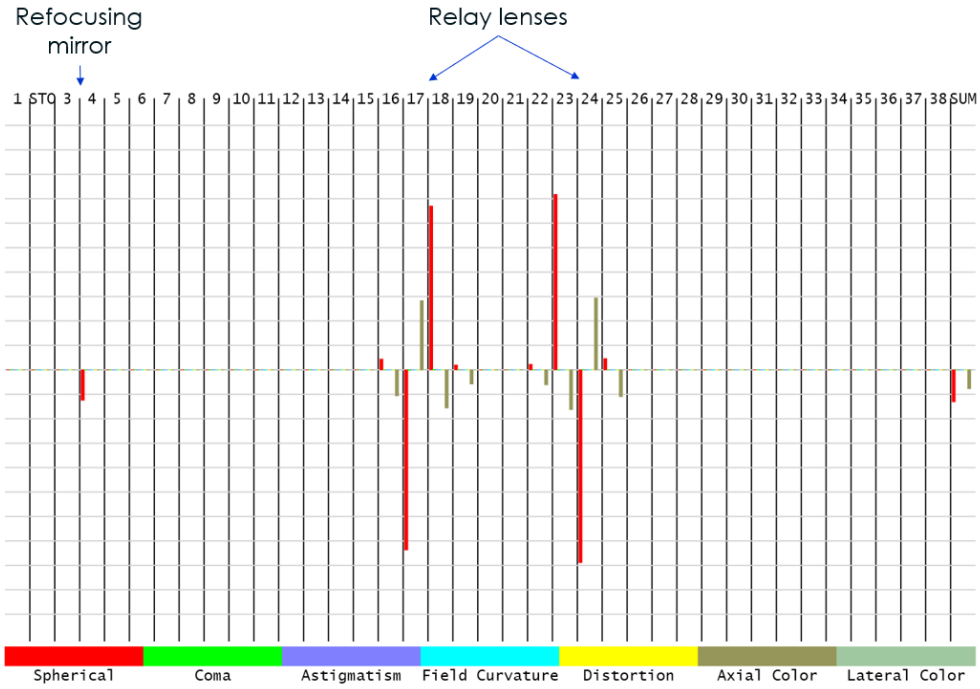

Figure S16. Seidel diagram of the HPD imaging system computed at the central wavelength of the laser 810 nm. The numbers listed at the top of the figure are the optical surfaces at which aberrations are calculated.

7. Laser pulse duration

Measurement of the laser pulse duration is done with a commercial frequency-resolved optical gating (FROG) single-shot second-order autocorrelator. The spectrum of a representative laser pulse given in Figure S17 shows the duration of the pulse that is optimized at the FROG location. The uncertainty of the pulse duration is (24 ± 1) fs.

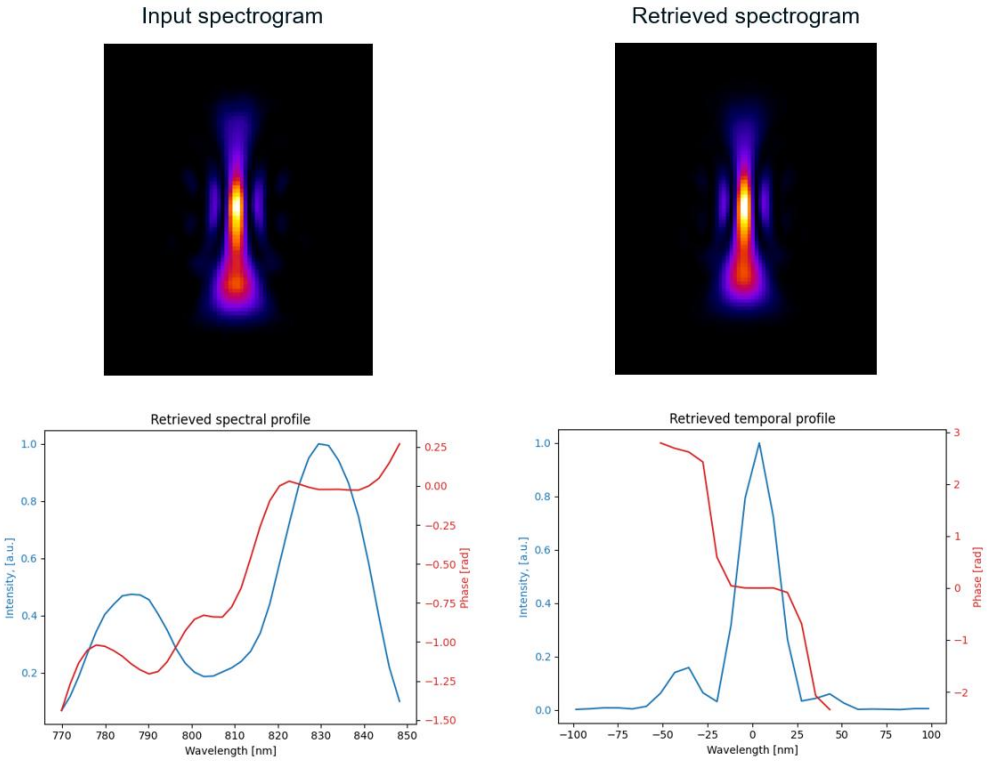

Figure S17. Retrieved duration of 24.4 fs (FWHM) for a representative laser pulse.

8. References

1. C. Radier, O. Chalus, M. Charbonneau, S. Thambirajah, G. Deschamps, S. David, J. Barbe, E. Etter, G. Matras, S. Ricaud, V. Leroux, C. Richard, F. Lureau, A. Baleanu, R. Banici, A. Gradinariu, C. Caldararu, C. Capiteanu, A. Naziru, B. Diaconescu, V. Iancu, R. Dabu, D. Ursescu, I. Dancus, C. A. Ur, K. A. Tanaka, and N. V. Zamfir, "10 PW peak power femtosecond laser pulses at ELI-NP," High Power Laser Science and Engineering **10**, e21 (2022).
2. F. Lureau, G. Matras, O. Chalus, C. Derycke, T. Morbieu, C. Radier, O. Casagrande, S. Laux, S. Ricaud, G. Rey, A. Pellegrina, C. Richard, L. Boudjemaa, C. Simon-Boisson, A. Baleanu, R. Banici, A. Gradinariu, C. Caldararu, B. D. Boisdeffre, P. Ghenuche, A. Naziru, G. Kolliopoulos, L. Neagu, R. Dabu, I. Dancus, and D. Ursescu, "High-energy hybrid femtosecond laser system demonstrating 2 × 10 PW capability," High Power Laser Science and Engineering **8**, e43 (2020).
3. O. Chalus, C. Derycke, M. Charbonneau, S. Pasternak, S. Ricaud, P. Fischer, V. Scutelnic, E. Gaul, G. Korn, S. Norbaev, S. Popa, L. Vasescu, A. Toma, G. Cojocaru, and I. Dancus, "High-contrast 10 PW laser system at the Extreme Light Infrastructure - Nuclear Physics facility," High Power Laser Science and Engineering **12**, e90 (2024).